 CMC, vol.26, no.1, pp.37-65, 2011

A New Inverse Algorithm for Tomographic Reconstruction of Damage Images Using Lamb Waves

M. Morii[1], N. Hu[1,2], H. Fukunaga[3], J.H. Li[1], Y.L. Liu[1], S. Atobe[3] Alamusi[3] and J.H. Qiu[4]

Abstract: Lamb wave tomography (LWT) is a potential and efficient technique for non-destructive tomographic reconstruction of damage images in structural components or materials. A new two-stage inverse algorithm with a small amount of scanning data for quickly reconstructing damage images in aluminum and CFRP laminated plates was proposed in this paper. Due to its high sensitivity to damages, the amplitude decrease of transmitted Lamb waves after travelling through the inspected region was employed as a key signal parameter related to the attenuation of Lamb waves in propagation routes. A through-thickness circular hole and a through-thickness elliptical hole in two aluminum plates, and an impact–induced invisible internal delamination in a CFRP laminated plate were used to validate the effectiveness and reliability of the proposed method. It was concluded that the present new algorithm was capable of reconstructing the images of the above mentioned various damages successfully with much less experimental data compared with those needed by some traditional techniques.

Keywords: Lamb wave tomography, inverse algorithm, damage image, attenuation.

1 Introduction

In order to improve the safety, reliability and operational life of various structures, the development of efficient techniques for non-destructive damage inspection is essential. Lamb wave tomography (LWT) is one of the efficient techniques, which has been used successfully in many applications ranging from material loss detection to borehole detection. This technique is to reconstruct a damage image by

[1] Chiba University, Chiba, Japan
[2] Chongqing University, Chongqing, China
[3] Tohoku University, Sendai, Japan
[4] Nanjing University of Aeronautics and Astronautics, Nanjing, China

illuminating an object in many different directions in the plane of interest using Lamb waves, which is similar to the computerized tomography in medical non-invasive diagnostics and seismology. Time-of-flight change and amplitude change of Lamb waves, which are related to the different wave velocities and wave attenuations when Lamb waves pass through the damaged regions, respectively, are the most commonly used signal parameters for tomographic image reconstruction, e.g., [Jansen and Hutchins (1990); Wright *et al.* (1997); Malyarenko and Hinders (2000)]. Up to date, many tomographic image reconstruction algorithms have been developed, which can be classified into the following two categories. One is series expansion methods using iteration algorithms, such as algebraic reconstruction technique (ART) [Gordon, Bender and Herman (1970); Malyarenko and Hinders (2001)] and simultaneous iterative reconstruction technique (SIRT) [Gilbert (1972); Leonard, Malyarenko and Hinders (2002); Rosalie *et al.* (2005)]. This type of methods is suitable for complex situations like ray bending and non-standard sampling geometry. However, it may not be computationally efficient since a lot of physical unknowns corresponding to all grids in the scanned region are needed to be updated iteratively in a large-scale system. The other category includes various transform methods, such as Fourier inversion [Stark *et al.* (1981)] and filtered back-projection technique [Hutchins, Jansen and Edwards (1993); Jansen, Hutchins and Mottram (1994)], which are fast and efficient but require precise sampling geometry.

In this paper, a new two-stage inverse algorithm with a small amount of scanning data, which is suitable for complex cases, such as non-standard sampling geometry and multiple damages, was proposed. Basically, the proposed method is similar to the first category, i.e., series expansion methods mentioned above. However, to improve the image reconstruction efficiency, in the first stage of the present method, two sets of the parallel scanning data along X-axis and Y-axis, respectively, were employed to approximately identify the possible damaged areas. Then, unlike ART or SIRT employing unknowns in all grids in the scanned area, in the second-stage of the present method, based on the scanning data in the first stage plus some oblique projection scanning data, the exact damage images were reconstructed by using the unknowns corresponding only to those grids located in the possible damaged areas identified in the first stage. Therefore, the number of unknowns decreased remarkably. Finally, these unknowns were obtained through a simple linear approximation system, which could be easily solved using the least-square method or the quadratic programming method. In this work, the amplitude decrease of Lamb waves was used as a key signal parameter to evaluate and to reconstruct the image of the damaged region since the amplitude change was more sensitive to the damage compared with the change of time-of-flight caused by the wave velocity change. Two aluminum plates with a through-thickness circular hole and a through-thickness elliptical hole, and a CFRP laminated plate with low-velocity impact-induced invisible internal delamination, were employed to validate the reliability of the present new method. This paper was organized as follows. In Section 2, by virtue of the two damages in the aluminum plates, the experimental apparatus and our proposed scanning method were described in detail. In Section 3 the present new algorithm was put forward with detailed explanations by referring to the two holes in the aluminum plates. Then, in Section 4, the reconstructed damage images for the circular hole and the elliptical hole in the aluminum plates were presented. Finally, in Section 5, the described method was extended to the impact-induced invisible internal delamination in the CFRP laminated plate and the capability of the present method was discussed in detail.

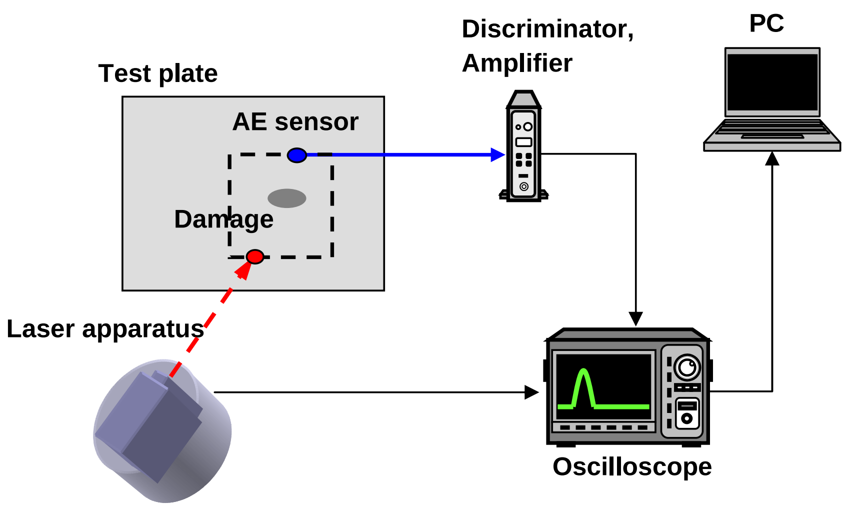

Figure 1: **Schematic diagram of experimental setup**

2 Experimental apparatus and scanning method

Figure 1 shows a schematic diagram of the experimental apparatus used in the present research. In this figure, there are the following main components in this experimental setup: laser (Japanese Laser Co. Ltd., lamp-pumped pulse YAG laser), acoustic emission (AE) sensor (NF Electronic Instruments, AE-903N), oscilloscope (Tektronix, TDS3034B), discriminator (NF Electronic Instruments, AE9922), amplifier (NF Electronic Instruments, 9917) and personal computer (DELL, CPU:

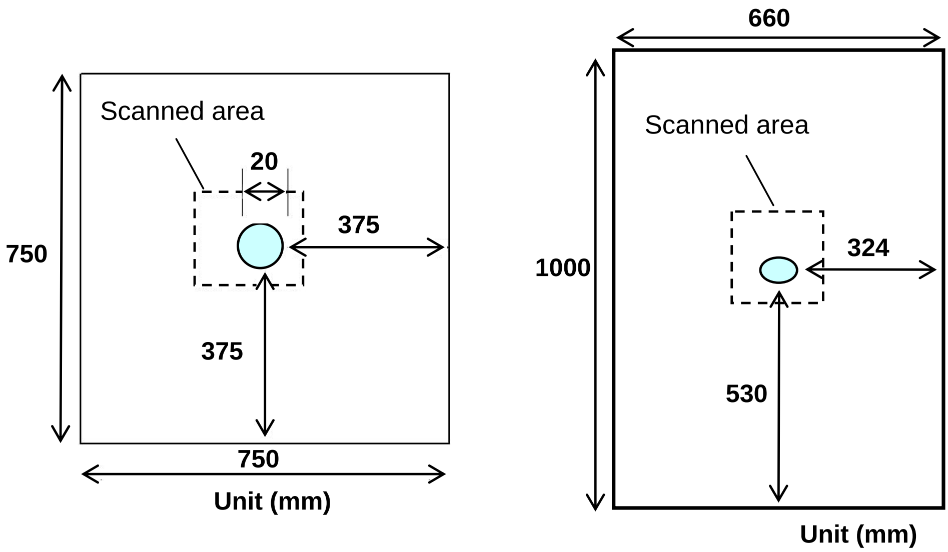

a) a circular hole b) an elliptical hole

Figure 2: **Test plates (: Damage, : Scanned region)**

Pentium III 1.0GHz). In this research, Lamb waves were excited by pulse laser irradiation. An AE sensor, which received wave signals, was attached on the plate. Both the laser irradiation and the AE sensor positions could be moved back and forth manually or by stepper motors controlled by the computer.

Firstly, in this section, two kinds of defects, i.e., a through-thickness circular hole and a through-thickness elliptical hole in two aluminum plates, were used to describe our scanning scheme and the inverse damage image identification algorithm. Figure 2(a) shows a square aluminum plate containing a circular hole of a diameter of 20 *mm* in the center. The thickness and side length of the plate were 5 *mm* and 750 *mm*, respectively. Figure 2(b) demonstrates a rectangular aluminum plate containing an elliptical hole with the minor-axis length of 12 *mm* and the major-axis length of 15 *mm*. The side lengths were 1000 *mm* and 660 *mm*, respectively, and thickness of the plate was 5 *mm*. The scanned areas for the two damages represented by dash lines shown in Fig. 2 for reconstructing the damage images were used.

Figure 3 demonstrates the damage geometry and scanning scheme in this research. Two squares of side lengths of 150 *mm* for the circular hole and 60 *mm* for the elliptical hole containing two defects were used as scanned areas as shown in Figs. 3(a) and 3(b), respectively. Two scanned square areas were divided into 30×30 grids and 24×24 grids with a side length of 5 *mm* for the circular hole and 2.5 *mm* for the elliptical hole, respectively. The four edges of the squares were named as A1, A2, B1 and B2, respectively. Some small solid black circles marked by numbers were located at the center of side edges of grids, which represented the locations of laser irradiation point (i.e., actuator) and sensor. In the current experimental setup, however, only two solid circle positions were occupied and used simultaneously since we used only one laser apparatus and one AE sensor.

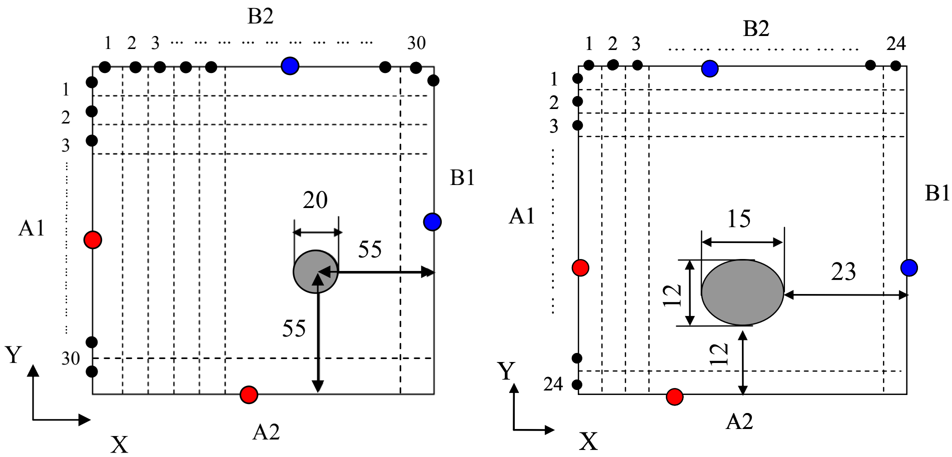

a) a circular hole b) an elliptical hole

Figure 3: **Damage geometry and scanning scheme**

Taking the case of circular hole as example (see Fig. 3(a)), for traditional ultrasonic inspections or LWT, e.g., cross-hole tomography using ART [Mckeon and Hinders (1999)], if only considering the rays from the left side to the right side, there are 30×30= 900 waveform data needed for the same experiment with the same size of grid spacing. To overcome the problem of a huge amount of experimental measurement data, in this research, only three sets of ray paths were designed for data acquisition as shown in Fig. 4. In this figure, four edges were defined as A1 and A2 for laser irradiation, and B1 and B2 for AE sensor, respectively. For each projection in Fig. 4(a), the laser irradiated along A1 or A2 edges, at the same time, the AE sensor moved on B1 or B2 edges in parallel, the set of these parallel path data was named as Set 1 in the following text. In Fig. 4(b), the laser irradiation point was fixed at the bottom of left corner (the 30^{th} position of A1 edge and the 1^{st} position of A2 edge), meanwhile, the AE sensor moved step by step along the opposite edge sweeping all available positions for data acquisition. This set of data was named as Set 2. In Fig. 4(c), firstly, the location of laser irradiation was fixed

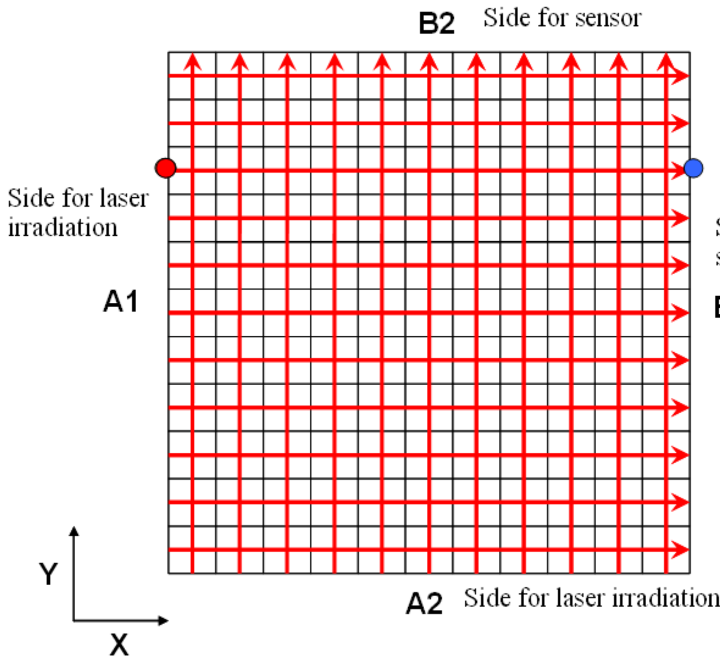

a) ray paths of Set 1 (circular hole)

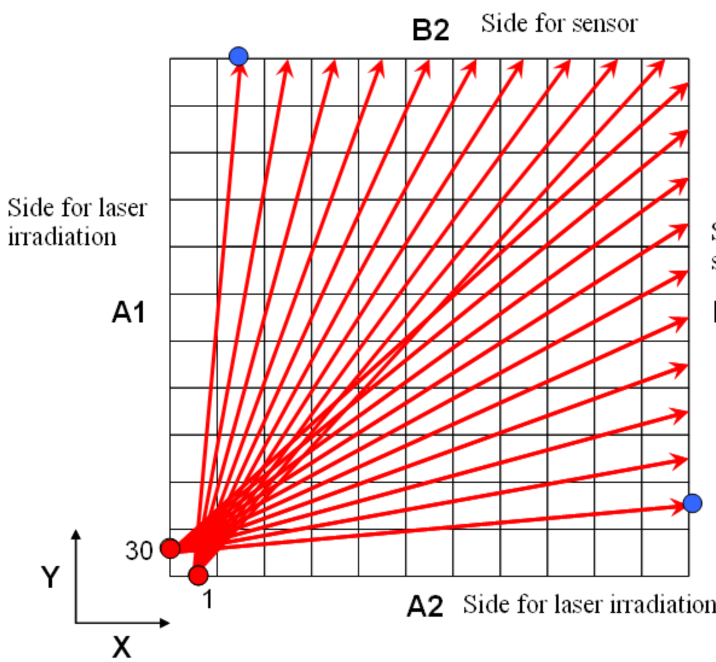

b) ray paths of Set 2 (circular hole)

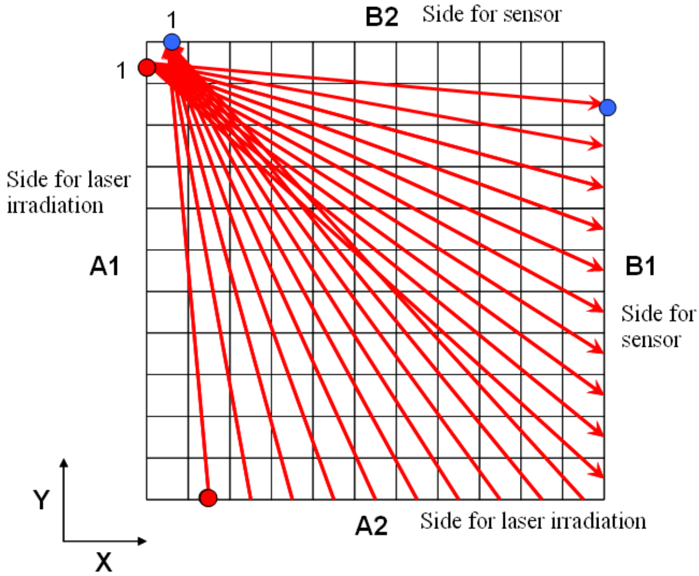

c) ray paths of Set 3 (circular hole)

Figure 4: **Scheme of data acquisition (●: laser irradiation position, ●: sensor position)**

at the 1st position of A1 edge, at the same time, the AE sensor stepped along the B1 edge sweeping all available positions. Then, by fixing the AE sensor at the 1st position of B2 edge, laser irradiated all available positions along the A2 edge. This set of data was named as Set 3. This new scanning scheme only needs 176 waveform data, which can save a lot of inspection time compared with that in the traditional techniques. Furthermore, the whole scanned area can be covered by the above scanning scheme.

For each ray path, after using the discriminator to filter out the signals either lower than 100 kHz or higher than 200 kHz for eliminating the noise as much as possible and using the amplifier to amplify the signal, the whole waveform was then input to the oscilloscope. Note that the frequency band of Lamb waves excited by the present pulse laser ranged mainly from 140 kHz to 180 kHz. Then, the signal was digitized and recorded by stacking it into a data file for analysis. Figure 5 presents a typical waveform received by the AE sensor on the B1 edge as the laser irradiated along the A1 edge in Set 1 in the intact region for the aluminum plate with the elliptical hole. Note that the first wave packet in Fig. 5 corresponds to the S_0 Lamb mode, which is very weak. The second wave packet of a strong

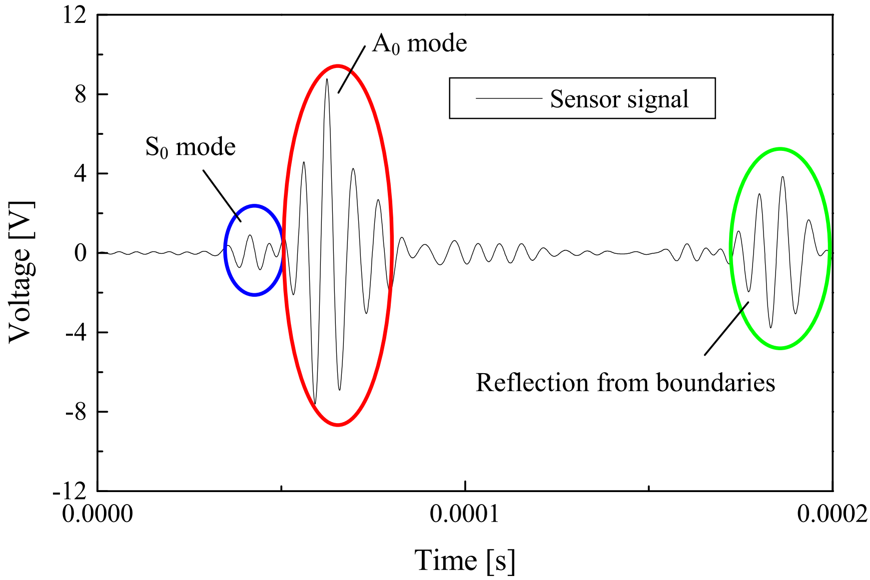

Figure 5: **Waveform of Set 1 from A1 to B1 in the intact region (elliptical hole)**

intensity corresponds to the A_0 Lamb mode. The wave packet after the second one represents the waves reflected from the boundaries or the damage of aluminum plate. After extracting the amplitudes of the second wave packet, i.e., the A_0 Lamb mode, in the waveforms of all ray paths, the reconstruction algorithm of damage image described in the following section was employed.

3 Image reconstruction algorithm

In this section, the algorithm for image reconstruction is described. The image reconstruction was carried out in two stages. In the first stage, the damage area and damage location were roughly identified by using the data of Set 1, i.e., parallel path data. In the second stage, then, the accurate damage shape was reconstructed based on the information of the first stage and the proposed inverse algorithm by making use of all experimental data (Set 1$\sim$3).

3.1 Approximate identification of damage location and area

Firstly, as shown in Fig. 6, the parallel path data of A1-B1 in Set 1 denoted by H_{1i} in turn, i.e., the data of the ray path parallel to X-axis from A1 edge to B1 edge, were used. H_{1i} was the wave amplitude at the sensor point of the ith ray path. The

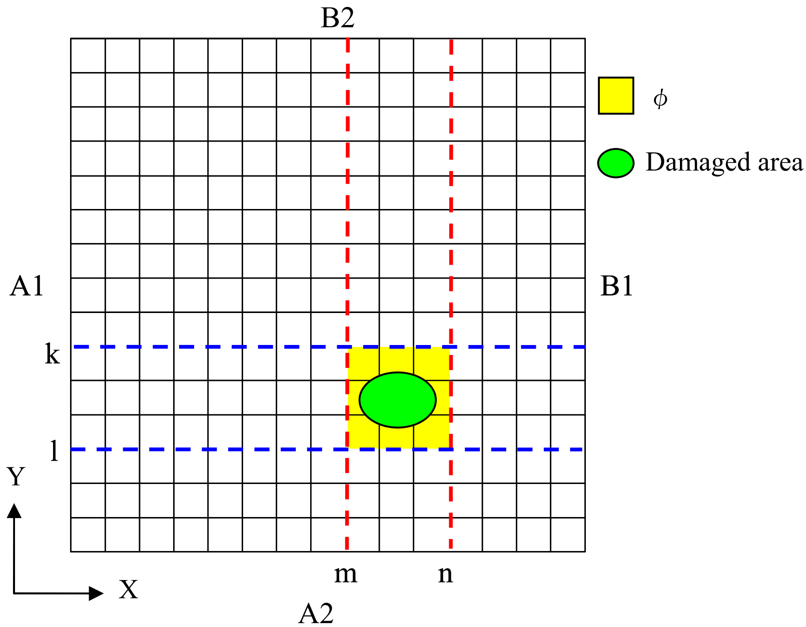

Figure 6: **Schematic view of scheme in the first stage (rough identification of damage area and location)**

average amplitude of A1-B1 parallel path data denoted by $\bar{H}_1$ can be expressed as:

$$\bar{H}_1 = \sum_{i=1}^{N} H_{1i}/N \tag{1}$$

where N is the number of parallel paths along X-axis.

Due to the amplitude decrease of waves passing through the damaged area, therefore, a threshold value α small than 1 was used in the following equation to select out those wave paths, which might pass through the possible damage area.

$$H_{1i} < \bar{H}_1 \times \alpha \tag{2}$$

When H_{1i} satisfies Eq. (2), it means that the wave in the ith ray path attenuates more severely, and its amplitude is smaller than the average value. Then it can be supposed that this ray path may pass through the damaged region. Figure 6 schematically shows the initial suspected region identified by using A1-B1 parallel path data of a plate containing a damage, which is the region from the k^{th} dash line to the l^{th} dash line.

Then, the A2-B2 parallel path data in Set 1 were processed by the same procedure stated above by using the following equations

$$\bar{H}_2 = \sum_{i=1}^{N} H_{2i}/N \tag{3}$$

$$H_{2i} < \bar{H}_2 \times \alpha \tag{4}$$

As shown in Fig. 6, the region identified by A2-B2 paths is from the m^{th} dash line to the n^{th} dash line, which partly overlaps the region surrounded by the k^{th} dash line and the l^{th} dash line. The overlapping region marked by ϕ is the rough area and location of the possible damage.

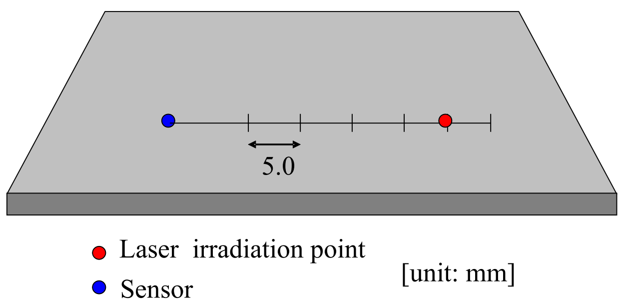

Figure 7: **Experimental model of the measurement of attenuation (aluminum plate)**

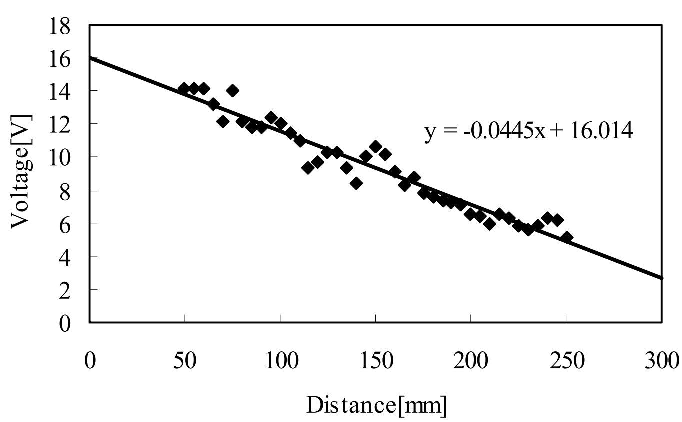

Figure 8: **Amplitude of Lamb wave versus propagation distance (aluminum plate)**

3.2 Accurate reconstruction of damage image

In general, the amplitude of A_0 Lamb wave mode decays with one upon square root of propagation distance. Especially, for a very short propagation distance, the wave amplitude decreases very fast. However, for a comparatively long propagation distance, we can assume that the amplitude decreases linearly when the wave propagates a distance δ as: $H_\delta = y - x \times \delta$. It means that when the wave propagates a distance of a unit length, the amplitude decrease ratio is x, i.e., attenuation coefficient of a Lamb wave mode (i.e., A_0 mode here). Note that y is the y-intercept of the line, which should be the wave amplitude H_0 at the wave source point if the wave decreases linearly in a rigorous form. However, as pointed previously, the wave amplitude decreases nonlinearly when the propagation distance is very small. Therefore, y is not strictly equal to H_0. However, in this work, for the sake of simplicity, we approximately assumed that y was equal to H_0.

By assuming that the attenuation coefficient in the intact region was x_I, and in the possible damaged region ϕ was x_i, respectively, firstly, x_I was measured by using the following experiment. As shown in Fig. 7, an intact aluminum plate with a sensor fixed on it was used. The laser irradiated along the straight line in Fig.7 at intervals of 5 *mm* meanwhile the sensor received the Lamb wave signal starting from the different excitation points. After the amplitude of each Lamb wave signal was obtained, as shown in Fig. 8, the relationship between propagation distance and the amplitude of Lamb wave was built up. In this figure, the distance between the sensor and the excitation point was taken as the x-axis, and the amplitude of Lamb wave was taken as the y-axis. In Fig. 8, the experimental data could be linearly approximated by a straight line, and then the *absolute value* of the slope of this line was used as the attenuation coefficient x_I, and the y-intercept was used as H_0.

As shown in Fig. 9, for an arbitrary ray path passing through the possible damaged region ϕ, the total change of the amplitude of Lamb wave can be linearly approximated as follows:

$$D_j = \sum_{i \not\subset \phi} L_i x_I + \sum_{i \subset \phi} L_i x_i \; (j = 1, 2, 3 \ldots, M) \tag{5}$$

where D_j is a positive value, which denotes the difference between the amplitudes of Lamb wave at the excitation point, i.e., H_0, and that at the sensor position along the jth ray path. L_i is the length that the jth ray path passes through the ith grid as shown in Fig. 9, and M is the total number of ray paths passing through the region ϕ. On the right-hand side of Eq. (5), the first term represents the sum of amplitude change due to attenuation when the wave passes through the grids out of

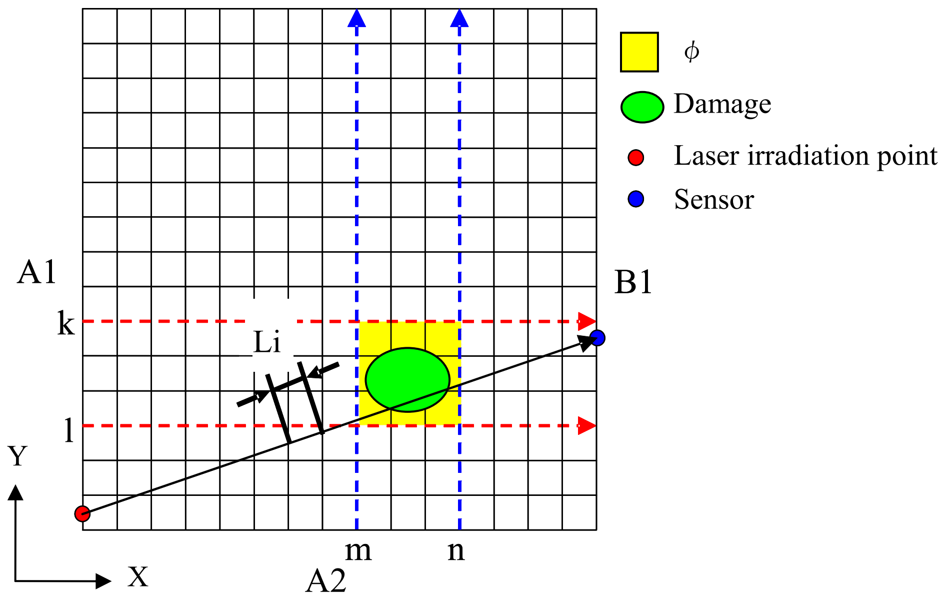

Figure 9: **Schematic view of the scheme for accurate reconstruction of damage image**

the possible damaged region ϕ, and the second term is the sum of amplitude change caused by the attenuation in the region ϕ.
Furthermore, x_i can be expressed as follows:

$$x_i = x_I + \Delta x_i \tag{6}$$

where Δx_i is the attenuation coefficient change of the ith grid in the region ϕ due to the possible damage, compared with the attenuation coefficient x_I of intact region.
Then, the following equation can be obtained by substituting Eq. (6) into Eq. (5),

$$\sum_{i\subset\phi} L_i \Delta x_i = D_j - \sum_{i\not\subset\phi} L_i x_I - \sum_{i\subset\phi} L_i x_I = f_j \; (j = 1,2,3\ldots,M) \tag{7}$$

The vector notation of Eq. (7) is expressed as:

$$\mathbf{S}\Delta\mathbf{x} = \mathbf{f} \tag{8}$$

which can be easily solved by using the least-square method as follows:

$$\Delta\mathbf{x} = (\mathbf{S^T S})^{-1}(\mathbf{S^T f}) \tag{9}$$

The above equation may yield both positive and negative values of Δx_i. However, physically, the result Δx_i should be positive for the damaged case (see Eq. (6)). Therefore, the above problem can also be reasonably solved by adding the corresponding constraint conditions on Δx_i as follows:

$$\begin{aligned} &\min \|\mathbf{S}\Delta\mathbf{x} - \mathbf{f}\| \\ &\quad \Delta x_i \geq 0 \end{aligned} \tag{10}$$

Eq. (10) can be easily solved by using the quadratic programming method [Goldfarb and Idnani (1983); Hu *et al.* (2001)] and the final results $\Delta\mathbf{x}$ (or Δx_i) can be obtained from the following equation:

$$\begin{aligned} &\min \tfrac{1}{2}\Delta\mathbf{x^T}(\mathbf{S^T S})\Delta\mathbf{x} - \mathbf{S^T f} + \mathbf{f^T f} \\ &\quad \Delta x_i \geq 0 \end{aligned} \tag{11}$$

After obtaining $\Delta \mathrm{x}_i$, the damage extents in various grids in the possible damaged zone can be represented by $\Delta \mathrm{x}_i$ and plotted to reconstruct the damage image in detail.

4 Results and discussions for two damages in aluminum plates

In this section the obtained damage images in the two aluminum plates is described and discussed in detail. Before performing the damage image reconstruction process, it is necessary to set up the proper threshold value of α in the first stage for approximately identifying the possible damage region, which is firstly explained in the following.

4.1 Threshold value α

In Section 3.2, there is a threshold value α in Eqs. (2) and (4) needed to be determined for roughly identifying the area and the location of damage. Basically, it is hopeful that the reconstructed image by using the proposed algorithm is insensitive to the choice of α. Therefore, the most sensitive signal parameter in waveform to damages should be used. Moreover, an appropriate threshold value α is very helpful to identify the approximate damage area and damage location efficiently, which leads to much smaller computational effort in the second stage of this algorithm. In this research, we explored two kinds of signal parameters, for discussing the choice of α in detail.

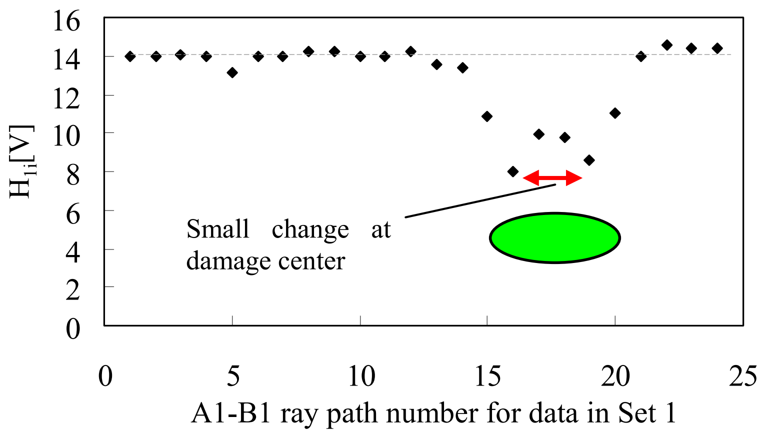

a) amplitudes of sensor signal for A1-B1 ray paths

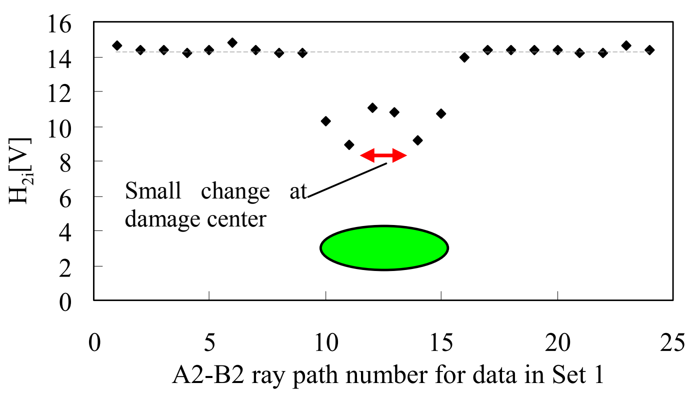

b) amplitudes of sensor signal for A2-B2 ray paths

Figure 10: **Amplitudes of Lamb waves for ray paths parallel to X and Y axes in Set 1 for the elliptical hole (: Position of hole)**

Firstly, as stated previously, we employed the amplitude of waveform. To assess the attenuation coefficient when Lamb waves pass through the damage, the amplitudes of Lamb waves with the ray paths parallel to X and Y axes in Set 1 are plotted in Fig. 10 for the case of elliptical hole, in which the horizontal axis denotes the ray path number from the top to the bottom, or from the left to the right of the plate (see Fig. 3(b)). From Fig. 10(a), we can observe that Lamb wave attenuates severely as the ray paths pass through the elliptical hole. The significant decrease of the amplitude of Lamb waves would be very effective to increase the sensitivity in damage inspection. The maximum changes of wave amplitude are around 43%

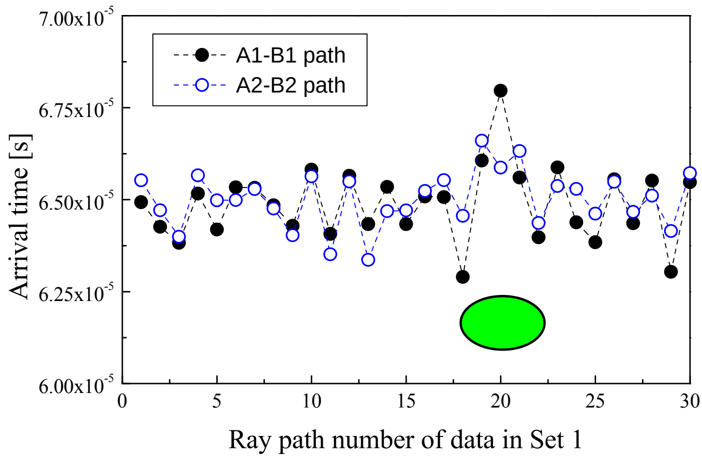

Figure 11: **Amplitudes of Lamb waves for ray paths parallel to X and Y axes in Set 1 for the circular hole (: Position of hole)**

when the wave passes through the edges of the elliptical hole. Note that for the ray paths of A2-B2 parallel to X-axis in Set 1 (see Fig. 10(b)), the same significant change of amplitude was also identified. Furthermore, it is interesting to note that in both figures, the amplitude change becomes smaller when the ray path passes through the center or near the center of the defect. This phenomenon is caused by wave diffraction. Usually, when the ray path passes the center of damage, the waves practically bypass the two sides of the damage, and then merge together, which leads to a smaller decrease of Lamb wave amplitude compared with ones passing the side edge of the defect. For the case of circular hole, the same significant amplitude decrease was also observed.

On the other hand, we also measured the arrival time of wave along A1-B1 and A2-B2 paths for the case of circular hole as shown in Fig. 3(a). The results of arrival time shown in Fig. 11 reflect the change of wave velocity when the wave passes through the defect. From this figure, it can be found that the change of arrival time is very small when the wave passes through the hole. The maximum change is only around 3.8%. Based on the above investigations, in this research, the amplitude of waveform was chosen. Moreover, in order to avoid the omission of possible damages or the reduction of real damage area size, a comparatively safe threshold value α for both holes was taken as 0.85 in the damage image reconstruction.

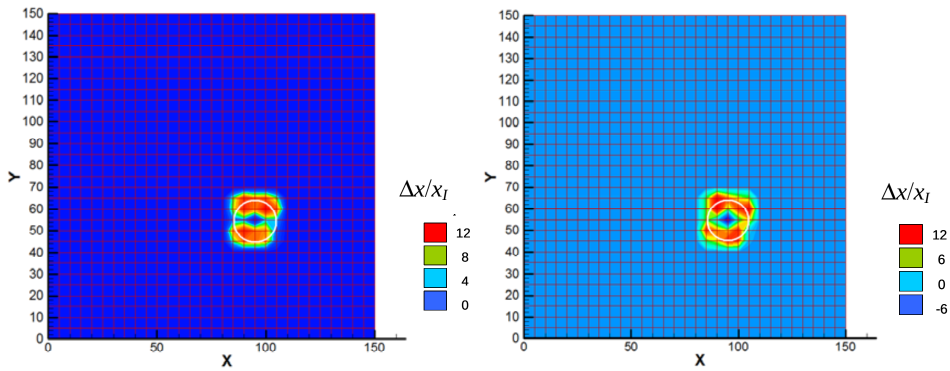

a) quadratic programming method b) least-square method

Figure 12: **Images of a circular hole**

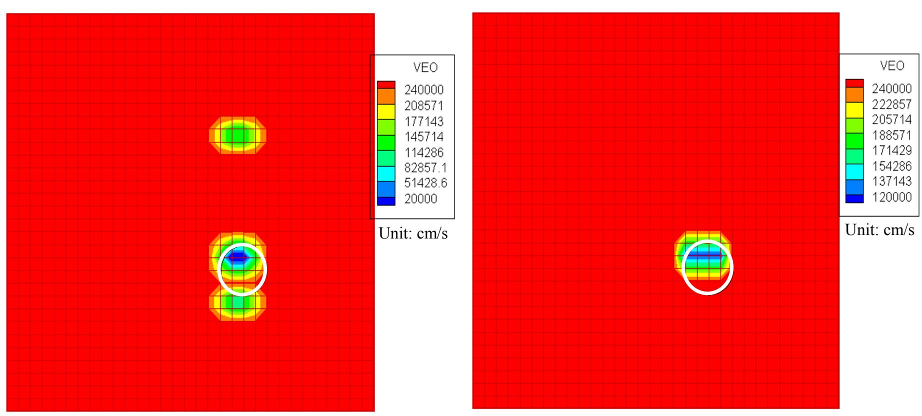

a) image result using velocity (α=1.012) b) image result using velocity (α=1.018)

Figure 13: **Images of circular hole when using arrival time as signal parameter**

4.2 Reconstructed damage images

When using all of the measured data, i.e., Set 1, Set 2 and Set 3 simultaneously, the reconstruction images of the circular hole in the aluminum plate are shown in Fig. 12. Note that the data of Set 2 and Set 3 were only used in this stage, i.e., the second stage. On the other hand, the data in Set 1 were used both the first stage and the second stage. After the first stage using the data in Set 1, the number of unknowns in 900 grids decreased from 30×30=900 to 25, i.e., the attenuation change Δx_i only in the possible damaged area. Therefore, it was very easy to identify them.

Figure 12(a) illustrates the results obtained from Eq. (11) by using the quadratic programming method, and Fig. 12(b) shows the results obtained from Eq. (9) by using the least-square method. In Fig. 12, the white circle represents the actual damage, and the various colors denote the ratio of attenuation change from the base attenuation in the intact region, i.e., $\Delta x/x_I$. From Figs. 12(a) and 12(b), it can be found that there is no obvious difference in the two kinds of results except that the damage image is smaller and clearer when using the quadratic programming method. Moreover, the ratio of attenuation change is negative in the center of the hole when using least-square method due to the smaller amplitude decrease as shown in Fig. 10. This result is physically unreasonable. Therefore, in the subsequent all examples, the quadratic programming method were continuously used. The location of damage was identified correctly in both results and the shape of damage was slightly distorted. This little distortion might be caused by the designed pattern of ray paths, which was not a symmetrical scanning scheme, or by the coarse grid spacing. Conclusively, the damage image could be reconstructed successfully in both results.

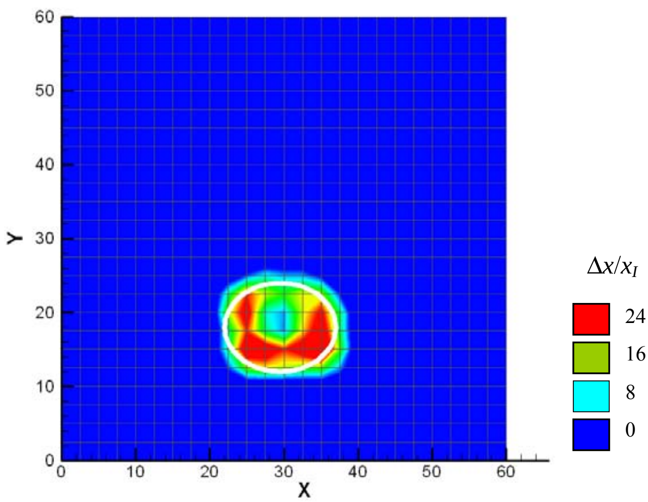

Figure 14: **Images of elliptical hole**

Furthermore, by using the arrival time, we also reconstructed the image of hole. In this case, it is necessary to replace Eqs. (2) and (3) using the following equations

$$T_{1i} > \bar{T}_1 \times \alpha, T_{2i} > \bar{T}_2 \times \alpha \tag{12}$$

in the first stage to identify the approximate damaged area and location, where the symbol "T" represents the arrival time.

Furthermore, by replacing x_i using $1/v_i$, x_I using $1/v_I$, and D_j using T_j, in Eqs. (5), (6) and (7), where v_I is the wave propagation velocity in the intact plate, which was 2400 *m/s* identified for the A_0 mode in our experiments, we obtained the variation of wave velocity. Note that the wavelet transformation on the wave signal and the arrival peak of transformed signal corresponding to the A_0 mode were used to identify the arrival time [Hu, Shimomukai, Fukunaga *et al.* (2008); Hu, Shimomukai, Yan *et al.* (2008)]. The obtained wave velocity is shown in Fig. 13 for two kinds of choices of α when using the quadratic programming method. In this figure, the reasonable result could be obtained when α=1.018 as shown in Fig. 13(b). However, it was quite tricky to choose a proper α. When α=1.012, multiple damages appeared as shown in Fig. 13(a). Therefore, it is quite difficult to use the arrival time of wave as signal parameter in our problems.

For the case of elliptical hole, the reconstructed image is shown in Fig. 14 when using the amplitude decrease of waveform and the quadratic programming method. The elliptical hole could also be successfully reconstructed.

5 Application to impact-induced internal delamination in CFRP plate

Delamination is one of the most common failure modes in composite laminates, and may be formed as a consequence of various impact events [Sekine and Hu (1998); Li, Hu, Yin *et al.* (2002); Li, Hu, Cheng *et al.* (2002)], poor fabrication processes and fatigue. As is well known, the compressive strengths of structures made from laminated composite materials may be severely reduced by the presence of this delamination damage [Hu (1999); Hu, Fukunaga, Sekine *et al.* (1999); Sekine, Hu and Kouchakzadeh (2000)]. Direct simulation of the internal delamination extension under impact loading is a tough task, which needs to tackle the numerical instabilities during the delamination propagation [Hu, Zemba, Fukunaga *et al.* (2007); Elmarakbi, Hu and Fukunaga (2009)], the possible multiple delamination [Hu, Sekine, Fukunaga *et al.* (1999)] and difficult dynamic contact problem [Hu (1997)]. In this section, the third example, i.e., low-velocity impact-induced delamination in a CFRP laminated plate, is described. To induce the internal delamination, the experiments were performed by the present authors using a weight-drop impact test machine of Dynatup 9250HD [Hu, Zemba, Okabe *et al.* (2008)]. The specimen of a quasi-isotropic CFRP laminated plate of 32 plies as $[(45^o/0^o/-45^o/90^o)_4]s$ was prepared according to the SACMA standard of CAI test. This plate was impacted by an impacting body of a lower semi-spherical shape and the mass of 4.6kg. The impact energy was 4.8J. For the same impact energy, experiments were carried out twice for two specimens. It is interesting to note that for the impact energy of 4.8 J, the delamination occurred only in one specimen, but did not occur in another one. Note that when the impact energy was 3.0 J, there was no

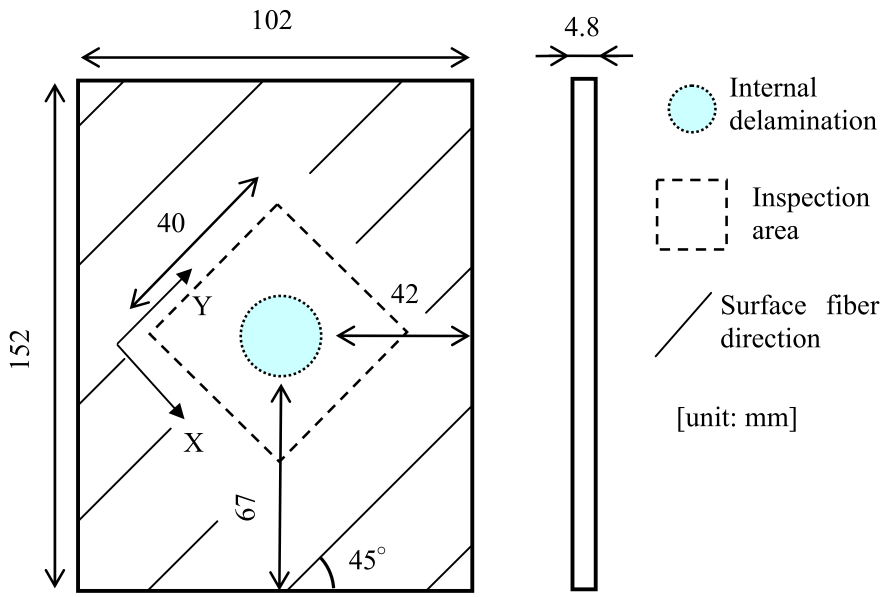

a) Front side of CFRP plate (impacted side)

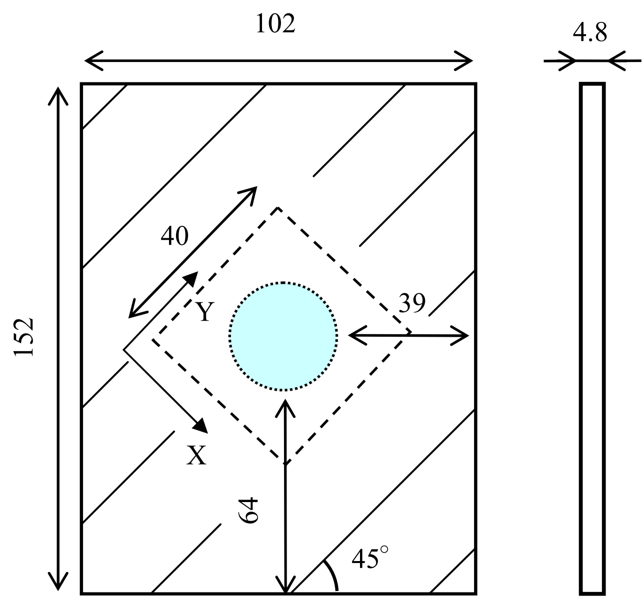

b) Back side of CFRP plate

Figure 15: **Dimensions for specimen and delamination reconstruction**

impact-induced delamination for any specimen. Therefore, the impact energy of 4.8 J can be thought of as the threshold of impact energy, which induces the possible internal delamination in CFRP laminates. In fact, this impact-induced internal delamination is seldom visible to the naked eye from the specimen surface. The ultrasonic inspection results of specimen after impact will be shown later. From the ultrasonic inspection result,it was found that the internal delamination area in the impacted side was smaller than that of the opposite side of impact. In this case, as explained later, since the wave attenuation strongly depends on the relationship between the wave propagation direction and the fiber direction of surface ply. For the convenience of calibration of wave attenuation coefficient, as shown in Fig. 15, we set up a local coordinate system (X-Y) according to the fiber direction of surface ply, and the inspection regions on the front side of CFRP plate (impacted side) and on the back side of CFRP plate were determined by referring to the internal delamination diameters identified by ultrasonic scanning inspection. The detailed scanning scheme is shown in Fig. 16 for the two surfaces.

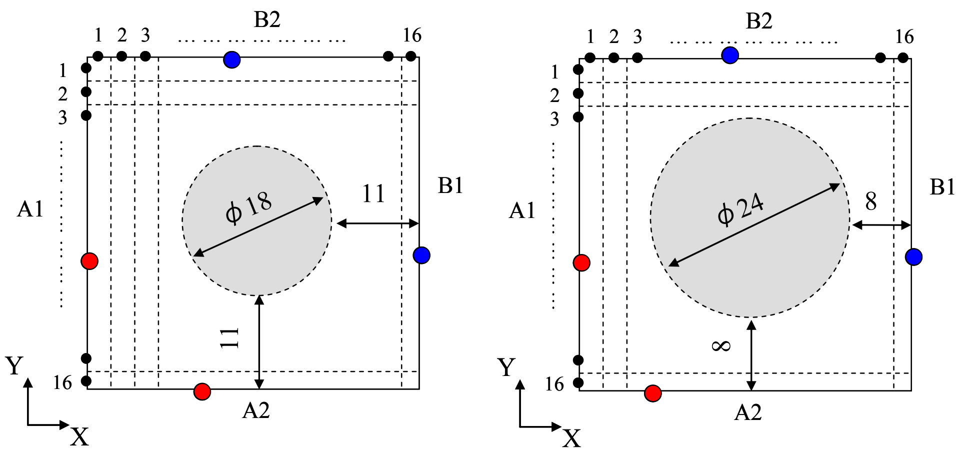

a) Front side of CFRP plate (impacted side) b) Back side of CFRP plate

Figure 16: **Detailed inspection schemes (● :Laser irradiation point; ● :Sensor ◌:internal delamination; unit: mm)**

The directly measured sensor signals for A1-B1 and A2-B2 ray paths on the back side of CFRP plate (see Fig. 16(b)) are shown in Fig. 17. From this figure, the significant decrease of wave amplitude can be identified. Similar to that observed in Fig. 10, the wave amplitude does not change significantly when the ray path is located near the center of the delamination. Moreover, by observing the y-axis of Fig. 17(a) and Fig. 17(b), it can be seen that the wave amplitudes for the same prop-

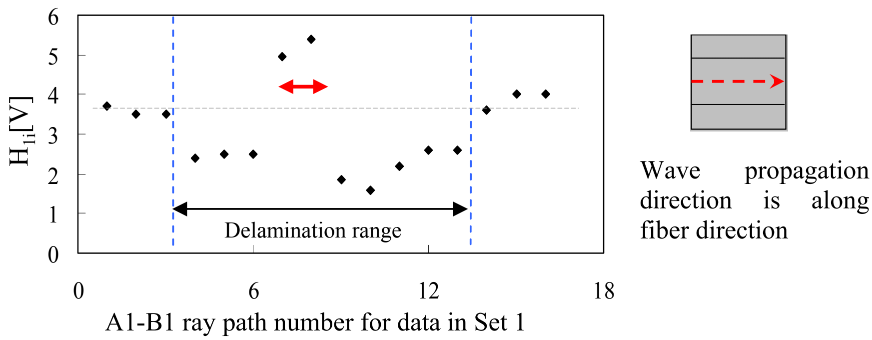

a) amplitudes of sensor signal for A1-B1 scanning

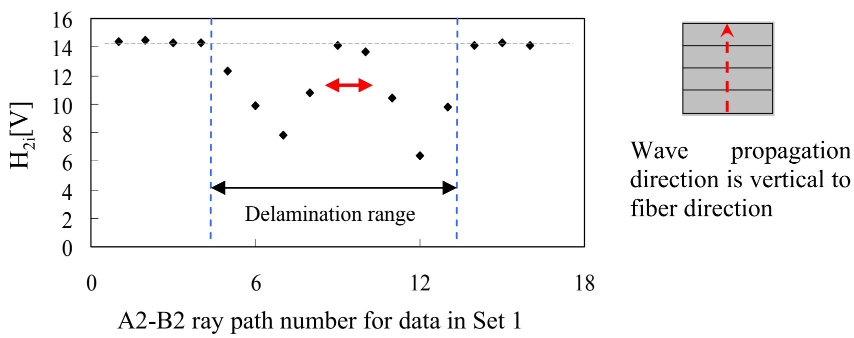

b) amplitudes of sensor signal for A2-B2 scanning

Figure 17: **Amplitudes of Lamb wave for ray paths parallel to X and Y axes in Set 1 for the back side surface of CFRP plate**

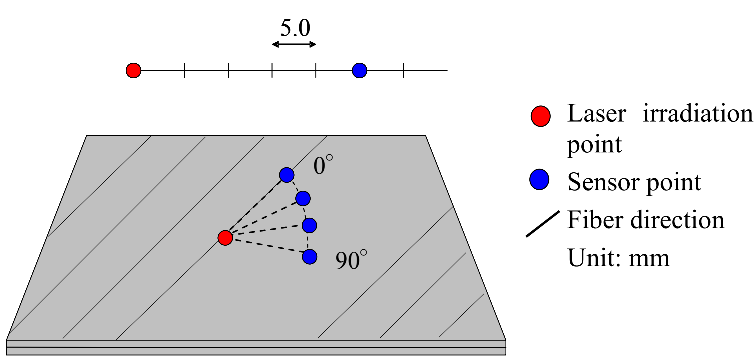

Figure 18: **Experimental model of the measurement of attenuation (CFRP plate)**

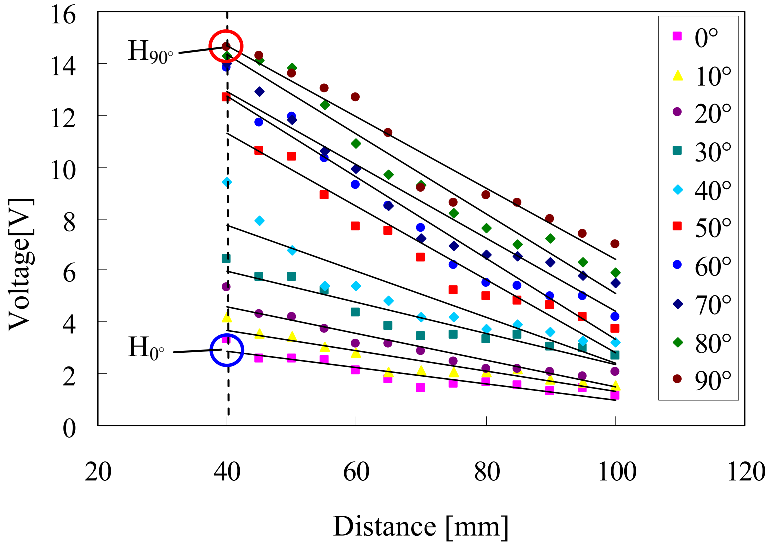

Figure 19: **Amplitude of Lamb waves versus propagation distance (5 mm increment) and propagation direction (10^o increment) in a CFRP plate**

agation distance are different when the wave propagates along the fiber direction or the vertical direction of fiber direction. Therefore, it can be considered that the wave attenuation coefficient varies with the angle between the wave propagation direction and the fiber direction of surface ply. To calibrate the wave attenuation coefficient along the different directions, an intact quasi-isotropic CFRP plate of the same stacking sequence as the specimens for impact tests, which was of a large size, i.e., 400 *mm*×400 *mm*, was used as shown in Fig. 18. The wave propagation direction was increased by the step size of 10^o from the fiber direction to the vertical direction of fiber direction. As shown in Fig. 18, the sensor was firstly put at the point being 40 *mm* away from the laser irradiation point, which was then moved step by step with the size of 5 *mm* in the wave propagation direction. This starting distance, i.e., 40 *mm*, was chosen for conveniently performing the evaluation of possible damage region in Eqs. (2) and (3) in the first stage since the inspection region size was 40 *mm* (see Fig. 15). The obtained results are shown in Fig. 19.

In Fig. 19, taking the wave amplitudes after 40 *mm* propagation in the intact CFRP plate as H_{0° and H_{90° for the wave propagation along the fiber direction and along the vertical direction of fiber direction, respectively, it can be found that H_{90° is much higher than H_{0°. By denoting the angle between the wave propagation direction and the fiber direction on the surface ply as θ, then, it can be estimated that the wave amplitude for θ=90^o at the wave source point (i.e., the *y*-intercept) is much higher than that for θ=0^o at the wave source point. The reason for this phenomenon is that the wave is excited by thermal expansion at the laser irradiation point. The much lower thermal expansion coefficient and much higher stiffness along the fiber direction (i.e., 0^o) leads to the much lower wave amplitude for θ=0^o at the wave source point compared with the case for θ=90^o. Moreover, it can be found that the slopes of various lines in Fig. 19 are also different. Then, the attenuation coefficients are different in the different wave propagation directions. In the vertical direction of fiber direction, the wave attenuates much more significantly due to the larger slope compared with that in the fiber direction. Therefore, it is necessary to consider this feature when performing the image reconstruction of delamination.

From Eqs. (2) and (3), we can obtain the following equation by using a parameter α being smaller than 1

$$H_{1i} < H_{0^\circ} \times \alpha \tag{13}$$

$$H_{2i} < H_{90^\circ} \times \alpha \tag{14}$$

Unlike those in the case of aluminum plates, note that $H_{0^\circ}$and H_{90°in the intact region were used instead of the average values in the scanned area (see Eqs. (2) and (4)). Similar to that stated previously for aluminum plates, from those H_{1i} and H_{2i} which satisfy the above two equations, the possible damaged region in the first stage can be obtained. In this example, we took $\alpha = 0.87$ for the front side surface, and $\alpha = 0.83$ for the back side surface, respectively. The schematic view of the identified possible damaged regions for the front and back side surfaces is shown in Fig. 20. From this figure, it can be seen that there are four possible independent regions ϕ for one side surface, which is reasonable by seeing Fig. 17 since the wave amplitude does not decrease significantly when the wave passes through the central area of delamination.

After finishing the first stage and obtaining the multiple possible damaged regions, the detailed damage image was reconstructed as follows.

By using θ (see Fig. 20), similar to Eq. (5), the total change of the wave amplitude after passing through the inspection area can be linearly approximated as:

$$D_j = \sum_{i \not\subset \phi} L_i x_\theta + \sum_{i \subset \phi} L_i x_i \; (j = 1, 2, 3 \ldots, M) \tag{15}$$

Similar to the case of aluminum plates, D_j is the difference between the amplitudes of Lamb waves at the excitation point denoted by H_θ, and that at the sensor position. x_θ is the attenuation coefficient of Lamb waves in the intact regions along the direction of θ, and x_i is the attenuation coefficient of Lamb waves in the possible

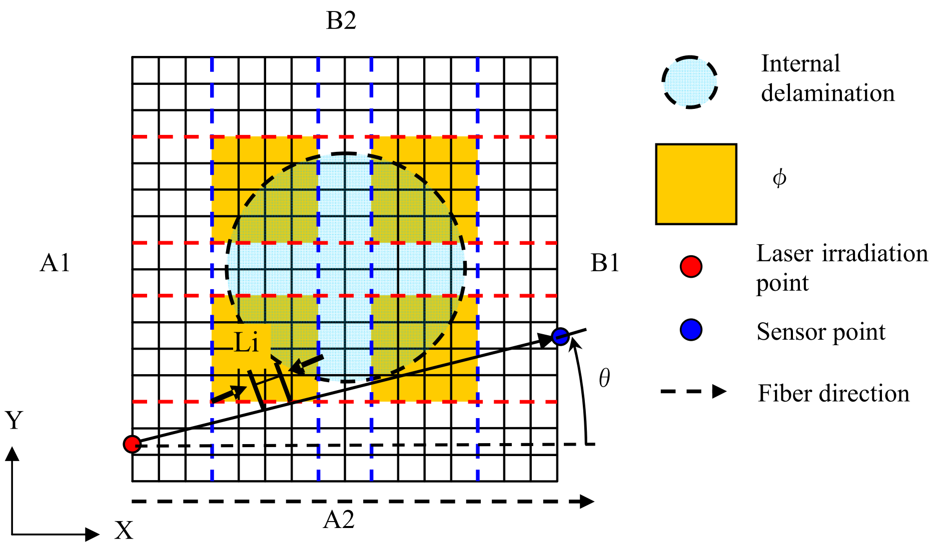

Figure 20: **Schematic view of possible damaged regions for front back sides**

damaged regions, i.e., grids in ϕ,.and L_i (see Fig. 20) and M are the same with those in Eq. (5).

As explained previously, the wave amplitude at the wave source point and wave attenuation coefficient depend on the angle between the wave propagation direction and the fiber direction, i.e., θ. Therefore, x_θ and H_θ vary with this angle θ. Here, an approximate approach was employed to tackle this problem based on the experimental data in Fig. 19 corresponding to various sampling angles with 10^o increment. For instance,

Table 1: Approximation of x_θ and H_θ

Range of angle	Approximation
$\theta = 0^\circ$	0°
$0^\circ < \theta \leq 15^\circ$	10°
$15^\circ < \theta \leq 25^\circ$	20°
$25^\circ < \theta \leq 35^\circ$	30°
......	......
$75^\circ < \theta < 90^\circ$	80°
$=90^\circ$	90°

when the ray path line just possessed an angle θ being the same with a sampling angle, e.g., 10^o, 20^o, etc., we simply obtained the slope and the y-intercept of a straight line corresponding to θ from Fig. 19, which were x_θ and H_θ, respectively. For a ray path line whose angle θ was located between two specified angles, as defined in Table 1, e.g., between 15^o and 25^o, we approximately employed x_θ and H_θ at a sampling angle, e.g., 20^o, which was the center of the above two specified angles, to represent the x_θ and H_θ of this ray path line. Similar to the case of aluminum plates, for the wave attenuation coefficient in the delamination area, we also used

$$x_i = x_\theta + \Delta x_i \tag{16}$$

to denote the change of wave attenuation coefficient. Note that in the possible damaged zone, we did not consider the influence of material anisotropy on Δx_i. For one grid in ϕ, there was only one Δx_i.

Similar to Eq. (7), from Eq. (16), finally we can obtain the following relationship

$$\sum_{i\subset\phi} L_i \Delta x_i = D_j - \sum_{i\not\subset\phi} L_i x_i - \sum_{i\subset\phi} L_i x_\theta = f_j \ (j = 1, 2, 3 \ldots, M) \tag{17}$$

Then, the similar equation of Eq. (8) can be constructed, which can be solved by using the quadratic programming method (Eq. (11)).

The final reconstructed delamination images for the front and back side surfaces are shown in Fig. 21, with the comparison of ultrasonic inspection images. Note that the obtained Δx_i was normalized by $\bar{x}_\theta$, which was the average value of x_θ ranging from $0^o$to 90^o obtained from Fig. 19. In this figure, for the present technique, the obtained delamination area on the back side surface of the laminates is larger than that in the front side surface of the laminates. The images of the low-velocity induced invisible internal delamination were reconstructed successfully by comparing with that of ultrasonic inspection. The present images are comparatively coarse due to the small specimen with the coarse inspection grid, i.e., 16×16 of 2.5 mm grid spacing (see Fig. 16). With a larger fine grid, it is expected that the detailed delamination image can be reconstructed.

6 Conclusions

A new two-stage inverse algorithm for fast reconstructing the image of the damage based on the LWT technique was presented in this paper. Compared with some traditional techniques, e.g., ultrasonic inspection in which the waves propagate along the specimen thickness direction, the present approach needs only a very small amount of experimental scanning data. The inspection region of the present technique can be quite large due to the long-distance propagation capability of Lamb

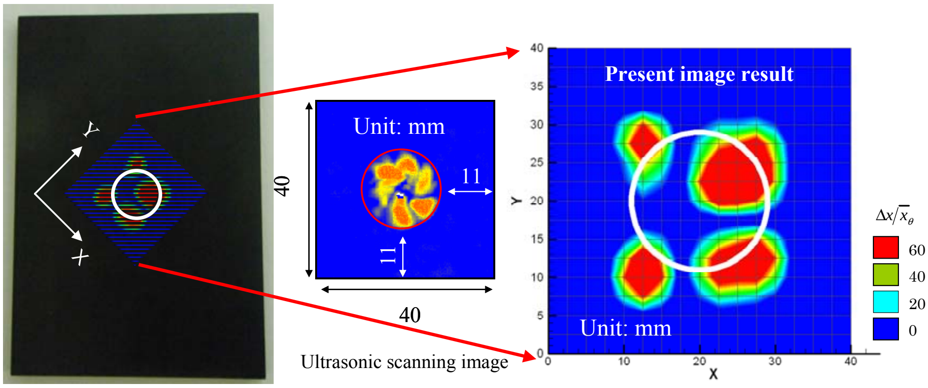

a) Front side of CFRP plate (impacted side)

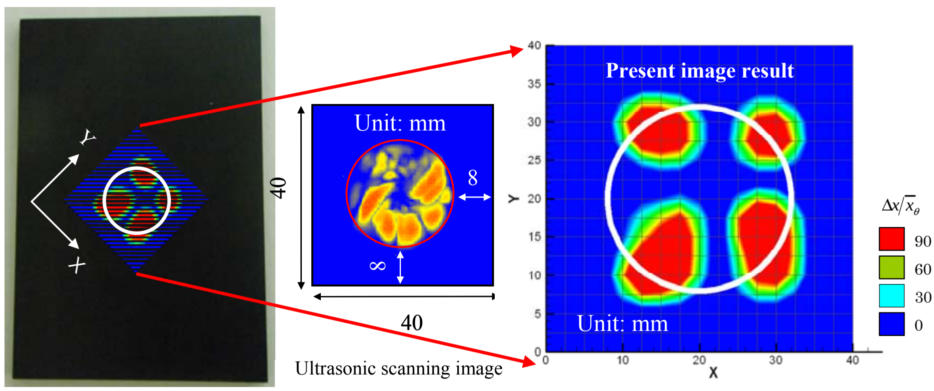

b) Back side of CFRP plate

Figure 21: **Reconstructed delamination images for front and back sides**

waves. In the first stage of the present approach, the possible damaged area and location were identified approximately by using two sets of parallel scanning data. Then, in the second stage, the damage parameters in small quantity, which only belonged to the grids in the possible damaged areas identified in the first stage, such as changes of wave attenuation coefficient or wave velocity, were computed by using a defined minimum problem from a linear approximation. Two aluminum plates with a hole and an elliptical hole were used to describe the present approach and to validate the reliability of the present method as test problems. The results show that it is much better to use the amplitude change of waveform as the signal parameter, i.e., the wave attenuation coefficient, for the damage image reconstruction since it is very sensitive to the existence of damages. Furthermore, a CFRP laminated plate with low-velocity impact-induced internal delamination was employed to verify the effectiveness of the proposed approach. The results demonstrate that it is necessary to obtain the wave amplitudes at the wave source point and the wave attenuation coefficients at the different wave propagation directions due to anisotropic material properties of CFRP laminated plate. By carefully dealing with this problem, i.e., the different wave amplitudes at the wave source point and different wave attenuations along various propagation directions, the invisible internal delamination was also reconstructed successfully by comparing with the results of ultrasonic inspection technique.

References

Alamusi; Liu, Y.L.;Hu, N. (2010): Numerical Simulations on Piezoresistivity of CNTPolymer Based Nanocomposites. *CMC: Computers, Materials & Continua*, vol. 20 no. 2, pp. 101-118.

Elmarakbi, A.; Hu, N.; Fukunaga, H. (2009): Finite element simulation of delamination growth in composite materials using LS-DYNA. *Compos. Sci. & Technol.*, vol. 69, pp. 2383-2391.

Gilbert, P. (1972): Iterative method for the three-dimensional reconstruction of an object from projections. *J. Theor. Biol.*, vol. 29, pp. 105-117.

Goldfarb, D.; Idnani, A. (1983): A numerically stable dual method for solving strictly convex quadratic programs. *Mathematical Programming*, vol. 27, pp. 1-33.

Gordon, R.; Bender, R.; Herman G.T. (1970): Algebraic reconstruction techniques for three-dimensional electron microscopy and X-ray photography. *J. Theor. Biol.,* vol. 29, pp. 471-481.

Hu, N. (1997): A solution method for dynamic contact problems. *Comput. & Struct.*, vol. 63, pp. 1053-1063.

Hu, N. (1999): Buckling analysis of delaminated laminates with consideration of contact in buckling mode. *Int. J. Num. Meth. Engrg.*, vol. 44, pp. 1457-1479.

Hu, N.; Fukunaga, H.; Sekine, H.; Kouchakzadeh, M.A. (1999): Compressive buckling of laminates with an embedded delamination. *Compos. Sci. Tech.*, vol. 59, pp. 1247-1260.

Hu, N.; Sekine, H.; Fukunaga, H.; Yao, Z.H. (1999): Impact analysis of composite laminates with multiple delaminations. *Int. J. Impact Engrg.*, vol. 22, pp. 633-648.

Hu, N.; Shimomukai, T.; Fukunaga, H.; Su, Z. (2008): Damage identification of metallic structures using A_0 mode of Lamb waves. *Struct. Health Monitoring: An*

Int. J., vol. **7,** pp. 271-285.

Hu, N.; Shimomukai, T.; Yan, C.; Fukunaga, H. (2008): Identification of delamination position in cross-ply laminated composite beams using S_0 Lamb mode. *Compos. Sci. Tech.*, vol. 68, pp. 1548-1554.

Hu, N.; Wang, X.; Fukunaga, H.; Yao, Z.H.; Zhang, H.X.; Wu, Z.S. (2001): Damage assessment of structures using modal test data. *Int. J. Solids Struct.*, vol. 38, pp. 3111-3127.

Hu, N.; Zemba, Y.; Fukunaga, H.; Wang, H.H.; Elmarakbi, A.M. (2007): Stable numerical simulations of propagations of complex damages in composite structures under transverse loads. *Compos. Sci. & Technol.*, vol. 67, pp. 752-765.

Hu, N.; Zemba, Y.; Okabe, T.; Yan, C; Fukunaga H.; Elmarakbi, A.M. (2008): A new cohesive model for simulating delamination propagation in composite laminates under transverse loads. *Mech. Mater.*, vol. 40, pp. 920-935.

Hutchins, D.A.; Jansen, D.P.; Edwards, C. (1993): Lamb wave tomography using non-contact transduction. *Ultrasonics*, vol. 31, pp. 97-103.

Jansen, D.P.; Hutchins, D.A. (1990): Lamb wave tomography. *Proc. of IEEE Ultrasonics Symp.*, pp. 1017-1020.

Jansen, D.P.; Hutchins, D.A.; Mottram, J.T. (1994): Lamb wave tomography of advanced composite laminates containing damage. *Ultrasonics*, vol. 32, pp. 83-98.

Leonard, K.R.; Malyarenko, E.V.; Hinders, M.K. (2002): Ultrasonic Lamb wave tomography. *Inverse Problems*, vol. 18, pp. 1795-1808.

Li, C.F.; Hu, N.; Yin, Y.J.; Sekine, H.; Fukunaga, H. (2002): Low-velocity impact-induced damage of continuous fiber-reinforced composite laminates. Part I. an FEM numerical model. *Compos. Part A*, vol. 33, pp. 1055-1062.

Li, C.F.; Hu, N.; Cheng, J.G.; Sekine, H.; Fukunaga, H. (2002): Low-velocity impact-induced damage of continuous fiber-reinforced composite laminates. Part II. verification and numerical investigation. *Compos. Part A*, vol. 33, pp. 1063-1072.

Malyarenko, E.V.; Hinders, M.K. (2000): Fan beam and double crosshole Lamb wave tomography for mapping flaws aging aircraft structures. *J. Acoust. Soc. Am.*, vol. 108, pp. 1631-1639.

Malyarenko, E.V.; Hinders, M.K. (2001): Ultrasonic Lamb wave diffraction tomography. *Ultrasonics*, vol. 39, pp. 269-281.

Mckeon, J.C.P.; Hinders, M.K. (1999): Parallel projection and crosshole contact scanning Lamb wave tomography. *J. Acoust. Soc. Am.*, vol. 106, pp. 2568-2577.

Rosalie, C.; Chan, A.; Chiu, W.K.; Galea, S.C.; Rose, F.; Rajic, N. (2005):

Structural health monitoring of composite structures using stress wave methods. *Compos. Struct.*, vol. 67, pp. 157-166.

Sekine, H.; Hu, N. (1998): Low-velocity impact response of composite laminates with a delamination. *Mech. Compos. Mater. & Struct.*, vol. 5, pp. 257-278.

Sekine, H.; Hu, N.; Kouchakzadeh, M.A. (2000): Buckling analysis of elliptically delaminated composite laminates with consideration of partial closure of delamination. *J. Compos. Mater.*, vol. 34, pp. 551-574.

Stark, H.H.; Woods, J.W.; Paul, I.; Hingorani, R. (1981): Direct Fourier reconstruction in computer tomography. *IEEE Trans. Acoust., Speech, Sig. Proc.* vol. 29, pp. 237-245.

Wright, W.; Hutchins, D.; Jansen, D.; Schindel, D. (1997): Air-coupled Lamb wave tomograph. *IEEE Trans Ultrason., Ferroelect. Freq. Contr.*, vol. 44, pp. 53-59.